Research Article | Vol. 10, No. 5 | 1 May 2019 | BIOMEDICAL OPTICS EXPRESS 2588
Biomedical Optics EXPRESS

Photoacoustic tomography for imaging the prostate: a transurethral illumination probe design and application

MIN AI,[1] JONG-IN YOUN,[2] SEPTIMIU E. SALCUDEAN,[1] ROBERT ROHLING,[1] PURANG ABOLMAESUMI,[1] AND SHUO TANG[1,*]

[1]*University of British Columbia, Faculty of Applied Science, Department of Electrical and Computer Engineering, 2332 Main Mall, Vancouver, V6T 1Z4, Canada*
[2]*Daegu Catholic University, College of Bio and Medical Sciences, Department of Biomedical Engineering, Gyeongsan-si, Gyeongbuk, 712702, South Korea*
**tang@ece.ubc.ca*

Abstract: *In vivo* imaging of prostate cancer with photoacoustic tomography is currently limited by the lack of sufficient local fluence for deep tissue penetration and the risk of over-irradiation near the laser-tissue contact surface. We propose the design of a transurethral illumination probe that addresses those limitations. A high energy of 50 mJ/pulse is coupled into a 1000-µm-core diameter multimode fiber. A 2 cm diffusing end is fabricated, which delivers light in radial illumination. The radial illumination is then reflected and reshaped by a parabolic cylindrical mirror to obtain nearly parallel side illumination with a doubled fluence. The fiber assembly is housed in a 25 Fr cystoscope sheath to provide protection of the fiber and maintain a minimal laser-tissue contact distance of 5 mm. A large laser-tissue contact surface area of 4 cm^2 is obtained and the fluence on the tissue surface is kept below the maximum permissible exposure. By imaging a prostate mimicking phantom, a penetration depth of 3.5 cm at 10 mJ/cm^2 fluence and 700 nm wavelength is demonstrated. The results indicate that photoacoustic tomography with the proposed transurethral probe has the potential to image the entire prostate while satisfying the fluence maximum permissible exposure and delivering a high power to the tissue.

1. Introduction

Prostate cancer (PCa) is the most common cancer and the second leading cause of cancer deaths among North American men [1]. Digital rectal examination (DRE) and serum prostate-specific antigen (PSA) are the current techniques for early detection of PCa. Upon a suspicious DRE and/or a high PSA reading, a transrectal ultrasound (TRUS) guided systematic random biopsy is performed [2]. If there is any PCa-positive biopsy core, a PCa diagnosis is confirmed. However, DRE is limited by a low overall sensitivity (37%) [3] and PSA is limited by a low specificity (36%) [4]. Because TRUS cannot identify PCa, the systematic sextant biopsy approach leads to repeated biopsies [5,6]. Meanwhile, various magnetic resonance imaging (MRI) techniques have been investigated for detecting PCa and show a consistently higher accuracy than conventional ultrasound (US) [7]. Combining various modalities, multi-parametric MRI (mpMRI) has the advantage of further increasing the accuracy. When mpMRI is available, it can be fused with US in order to guide some of the biopsy sampling to areas that appear suspicious on mpMRI [8]. However, unavoidable movements of the prostate affect the US-MRI registration and therefore lead to biopsy localization error [9,10]. Regardless of the techniques, since not all prostate tissue is sampled, there could be underestimation of the Gleason score which is related to PCa aggressiveness used in PCa patient management [6].

#359020 https://doi.org/10.1364/BOE.10.002588
Journal © 2019 Received 1 Feb 2019; revised 9 Apr 2019; accepted 10 Apr 2019; published 26 Apr 2019

Biomedical Optics EXPRESS

The limitations of the current diagnostic tools reflect a need for a better detection method which can realize targeted biopsy or even PCa diagnosis through *in vivo* imaging. Meanwhile, the key role of angiogenesis has been revealed in cancer growth and development in prostate and higher microvessel density (MVD) has been reported as a potential prognostic indicator in PCa [11]. This makes tumor angiogenesis a prospective objective for the detection of PCa, which leads to a wide range of new techniques in US [12] and MRI [9] for angiogenesis imaging. For US, both Doppler US and dynamic contrast-enhanced US (DCE-US) have been reported to be capable of monitoring the increase of MVD [11]. However, Doppler US only has high sensitivity to lesions with high Gleason score because Doppler US cannot detect microvessels but only large tumor feeding vessels [9]. The procedure of imaging prostate by DCE-US is time-consuming which limits its application for targeted biopsy [12]. Dynamic contrast enhanced MRI (DCE-MRI) has also been reported to image microvessel vascularity in prostate tissue [13]. As prostate is already highly vascularized, DCE-MRI has difficulty in discriminating cancer from prostatitis in the peripheral zone and from the high vascularized benign prostate hyperplasia [14].

Photoacoustic tomography (PAT) is an emerging imaging technique with a potential for PCa detection [15]. The photoacoustic (PA) signal in biological tissue originates from optical absorption in endogenous molecules such as hemoglobin. Upon illumination by a short laser pulse, an acoustic pressure wave is generated due to laser heating and thermal-elastic expansion in tissue. The acoustic wave then propagates towards the tissue surface over the depth that is determined by the acoustic attenuation inside the tissue [16]. The detection of the PA signal can be achieved by using a commercial US system which allows dual-modality imaging that includes both optical and ultrasonic contrasts. Previous studies have been carried out using PAT for the detection of PCa and the localization of brachytherapy seeds [17–22]. In 2003, Andreev *et al*. reported PAT imaging of human PCa *ex vivo*, which showed that the contrast difference between normal prostatic tissue and cancerous tissue was sufficient to locate tumors [17]. In another study, Wang *et al*. demonstrated non-invasive PAT imaging on canine prostate *in vivo* [18]. A lesion at 10 mm depth was imaged with high sensitivity and contrast-to-noise ratio. In 2016, Ishihara *et al*. published the work of PAT imaging on human prostate *in vivo* [19]. The system was designed to detect microvascular structures such as the neurovascular bundle and cancer angiogenesis for assisting the procedure of radical prostatectomy or targeted biopsy. A TRUS probe (6.5 MHz center frequency, 128 element linear array) was used to receive both PA and US signals. The illumination part delivered 60 mJ/pulse energy at 765 nm wavelength from two convex apertures integrated with the TRUS probe [20]. The estimated fluence on the tissue surface was 11 mJ/cm^2. The PA signal was obtained from a depth of 17 mm. However, the strong signal near the rectal wall caused by the high surface fluence hindered the discrimination of the signal from the neurovascular bundle in the same region. With the same system, Ishihara *et al*. further demonstrated the feasibility of imaging PCa angiogenesis by correlating the PA signal intensity to the total vascular area and total vascular length for prostate cancer [20]. Although the results need to be further confirmed due to the small number of patients, this pilot study shows that PAT has a great potential to image PCa.

The clinical translation of PAT to prostate intervention still has many challenges. The amplitude of PA signal is proportional to the local fluence which determines the penetration depth and the signal-to-noise ratio (SNR). Therefore, high irradiation energy is always desired in PAT imaging. In the reported systems [21,22], the integration of light delivery with the TRUS probe has the drawback of light attenuation by the rectal wall. Compared to transrectal illumination, theoretical analysis has shown that transurethral illumination could improve the light delivery [23,24]. It is more efficient for light to reach the entire volume of the prostate from its center through the urethral tube, than from the rectum. PAT with transurethral illumination was demonstrated in experiment by Bell *et al*. to image brachytherapy seeds and tested in canine prostate *in vivo* [25]. Using a 1000-μm-core diameter fiber, up to 8 mJ/pulse

Biomedical Optics EXPRESS

energy at 1064 nm wavelength was delivered. The fiber tip was polished at 45° angle and together with an end mirror at 45° angle light was directed to side illumination. The fiber and end mirror were housed in a 2 mm diameter quartz tube. The beam size on the tube surface was calculated to be 1.7 mm^2 which was very small and resulted in a high fluence on the tube surface [25]. The fiber with the quartz tube was then inserted into a urinary catheter, which increased the distance between the fiber and the tissue surface as well as the illumination area on the laser-tissue contact surface. For a 5.3 mm diameter urinary catheter, the authors estimated the fluence on the tissue surface to be below 99 mJ/cm^2 [25], which was just below the safety limit of 100 mJ/cm^2 at 1064 nm wavelength for skin.

For translating PAT to clinical applications, the laser safety limit needs to be addressed. In fact, the value of laser safety limit depends on the wavelength and radiation duration. Thermal effect that can cause tissue damage is a main concern while using visible and near infrared light. For a single pulse with pulse duration less than 100 ns, the maximum permissible exposure of fluence, $MPE_{fluence}$, is defined as [26],

$$MPE_{fluence} = \begin{cases} 20\times10^{2(\lambda-0.7)}\ \text{mJ/cm}^2 & (0.7\mu m \le \lambda \le 1.05\mu m) \\ 100\ \text{mJ/cm}^2 & (1.05\mu m \le \lambda \le 1.4\mu m) \end{cases}, \quad (1)$$

where λ is the wavelength. The MPE value decreases exponentially as the wavelength decreases and the $MPE_{fluence}$ value is as low as 20 mJ/cm^2 at 700 nm. When the accumulated exposure time by multiple pulses is longer than 10 s, the maximum permissible exposure in terms of average power, MPE_{power}, is defined as [26],

$$MPE_{power} = \begin{cases} 0.2\times10^{2(\lambda-0.7)}\ \text{W/cm}^2 & (0.7\mu m \le \lambda \le 1.05\mu m) \\ 1\ \text{W/cm}^2 & (1.05\mu m \le \lambda \le 1.4\mu m) \end{cases}. \quad (2)$$

Here the average power is the product of the repetition rate and the energy per pulse. Both the requirements on MPE_{power} and $MPE_{fluence}$ defined in Eqs. (1) and (2) should be satisfied in order to meet the safety standard. The laser safety limit and the demand for high energy output and for high SNR need to be considered together when designing an optimal illumination in PAT.

In this paper, a transurethral illumination probe is reported for PAT imaging of PCa. The probe contains a radial-illumination diffusing fiber, and a cylindrical mirror to reflect and shape the beam profile to one side. A method is proposed to fabricate the diffusing fiber to achieve radial firing over a few centimeters length of the fiber. A 3D printed silver mirror with cylindrical parabolic surface is integrated with the fiber to increase the fluence on one side for deeper penetration. Meanwhile, the fluence on the laser-tissue contact surface is controlled to be under the MPE value. The probe is tested on a tissue phantom which mimics the optical properties of human prostate. A 3.5 cm optical penetration depth is achieved which meets the need to image the entire prostate.

2. Design of the transurethral illumination probe

In our previous work, a scheme of delivering high energy laser pulses through a multimode fiber was described [27]. A cross cylindrical lens array was placed before the input end of the fiber to homogenize the incident beam, which led to high energy coupling and delivery. A high energy of 50 mJ/pulse was coupled into a 1000-μm-core diameter multimode fiber. Here the goal of the illumination probe design is to fully utilize the high output energy while keeping the fluence on tissue to be within the safety limit for both single pulse and long duration exposure.

Biomedical Optics EXPRESS

2.1 Configuration of the probe

The transurethral illumination probe design is shown in Fig. 1(a). A 1000-μm-core diameter multimode fiber (Thorlabs, Newton, New Jersey, United States) is fabricated to diffuse light from its side surface. The fiber is held by a 3D-printed plastic mount. To increase the fluence and realize side-firing, the light emitting from the diffusing fiber is directed to one side of the probe by a cylindrical reflection mirror constructed by 3D-printing. The mirror is glued with the fiber mount where the fiber is aligned to the focus of the cylindrical mirror. A 45° reflection surface at the end of the cylindrical mirror reflects and re-uses the remaining light emitted from the forward direction of the fiber tip to the side direction also. The assembled fiber is then inserted into a 25 Fr cystoscope sheath (8.33 mm diameter). The cystoscope sheath can support and protect the optical components when the probe is inserted in the urethra. Figure 1(b) shows a photograph of the transurethral illumination probe. Visible light at 660-nm wavelength is coupled into the fiber to display the beam profile. Figures 1(c) and 1(d) show the longitudinal and axial views, respectively, of the probe design. The coordinate axes are depicted in Fig. 1(d), where y is along the long direction of the probe, x is the perpendicular direction of the probe, and z is the direction of light propagation in the side illumination. The origin of the coordinate system is defined at the center of the fiber.

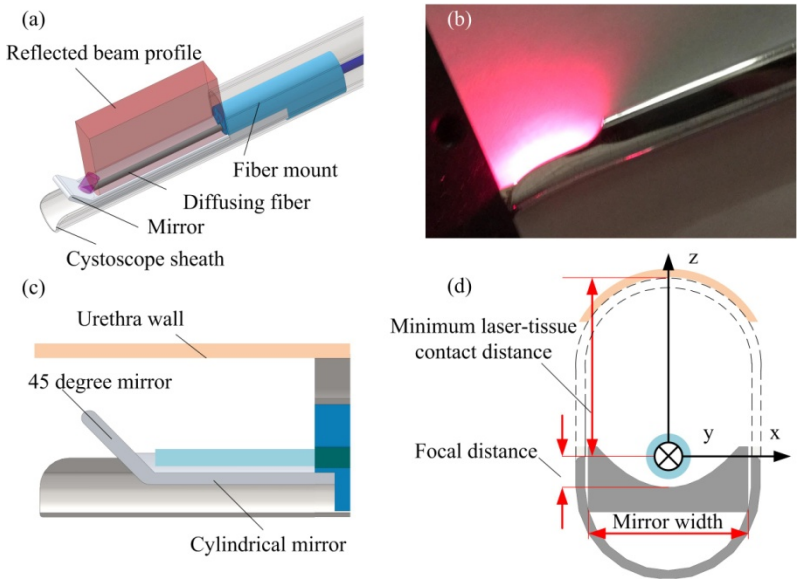

Fig. 1. Design of the transurethral illumination probe. (a) Overview of the transurethral illumination probe. (b) The beam profile from the probe displayed by a 660 nm light. (c) Longitudinal cross-section view of the probe. (d) Axial cross-section view of the probe.

Two different shapes of the cylindrical mirror have been investigated, a circular cylindrical mirror and a parabolic cylindrical mirror. Using the defined coordinates, the surface of the circular cylindrical mirror can be expressed as,

$$\left(z-\frac{r}{2}\right)+x^2=r^2 \tag{3}$$

where r is the radius of the circular cylinder. Under paraxial approximation, the focus of the circular cylindrical mirror is a line parallel to y-axis and its focal distance is $f_{circular}=r/2$. Similarly, the surface of the parabolic cylindrical mirror can be written as,

Biomedical Optics EXPRESS

$$z = \frac{x^2}{2p} - \frac{p}{2} \tag{4}$$

where its focal distance is $f_{parabolic} = p/2$.

The rigid surface of the cystoscope sheath supports the urethra wall and can avoid direct contact between the urethra wall and the optical fiber. The distance between the top surface of the cystoscope and the fiber is regarded as the minimal laser-tissue contact distance, e.g. a 25 Fr cystoscope sheath can provide ~5 mm laser-tissue contact distance. In the following sections, the design and analysis of the probe will be described in details.

2.2 Fabrication of the diffusing fiber

The normal size of a healthy prostate is approximately 25 ml in volume, or $3\,\text{cm} \times 5\,\text{cm} \times 3\,\text{cm}$ in the anterioposterior, transverse, and cephalocaudal prostate diameter, respectively [28]. With advancing age, the prostate size increases and varies in a wide range [29,30]. For imaging the prostate, the illumination pattern of the transurethral illumination probe should match the cephalocaudal dimension along the urethra. Thus, a diffusing fiber that can provide side illumination over a few centimeters length is required.

Several approaches have been reported to process a diffusing fiber. Mechanical processing methods [31,32], such as laser micro-machining and abrasion by sandpaper, have a risk to break a denuded fiber during the process. Also, manual abrasion by sandpaper requires experience to achieve the uniform roughness of the diffusing fiber. Meanwhile, Kosoglu *et al.* demonstrated an etching process and obtained a micro-needle of 33 µm diameter and 3 mm length by immersing a 105-µm-core diameter multimode fiber in 50% hydrofluoric acid for 50 minutes [33]. However, the replication of this approach on 1000-µm-core diameter multimode fiber is problematic. It takes much longer to etch the fiber due to the larger core size. Moreover, the etched fiber becomes very fragile since the core size is reduced significantly.

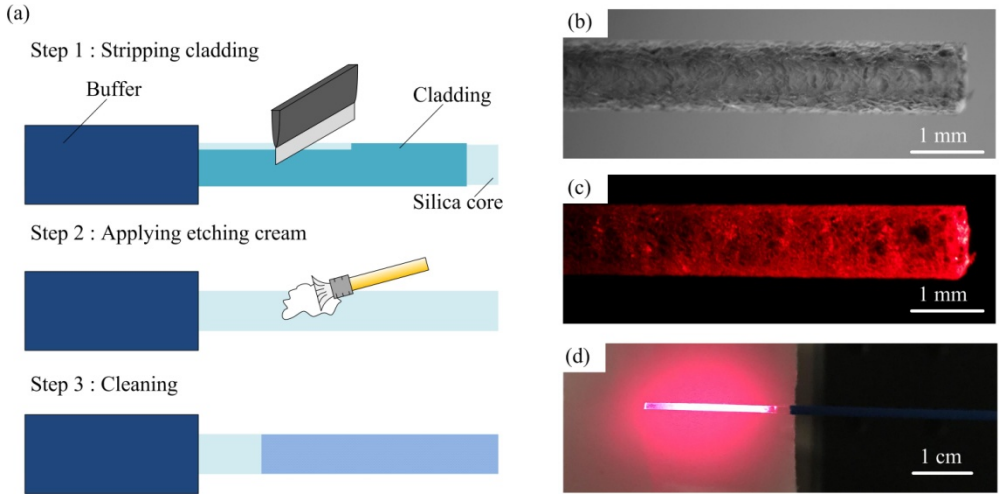

Fig. 2. Schematic illustration of the etching process (left) and photographs of the diffusing fiber (right). (a) Three steps of the etching process. (b) Rough surface of the diffusing fiber. (c) The diffusing fiber with 660 nm visible light coupled in. (d) Illumination pattern on a piece of white paper of the 660 nm light from the diffusing fiber.

To improve the etching process suitable for large core fiber, we have developed a process using glass etching cream (Armour etch, Armour Product, New Jersey, United States) to process large-core-diameter fiber and create a long section of diffusing fiber. Figure 2(a)

Biomedical Optics EXPRESS

illustrates the procedure in three steps. First, the buffer of the multimode fiber is removed by a stripper. The entire circumference of the cladding is scratched and removed by a sharp knife because the cladding layer does not react with the etching cream. In step 2, the bare fiber is etched by the etching cream for nearly 4 hours. Due to the slow reaction rate, the diameter of the bare fiber changes only slightly even after the long etching duration. At last, the cream is washed out by water and an irregular rough surface is formed as shown in Fig. 2(b). The etched fiber diffuses light circumferentially in 360° angles. Compared with the etching process by hydrofluoric acid, our process is moderate which only creates roughness on the side surface of the fiber without greatly reducing the core size. As a result, the etched part does not break easily. By coupling visible light at 660-nm into the fiber, the diffusing fiber shows a radial light illumination pattern along the etched surface as shown in Fig. 2(c). Figure 2(d) shows the diffusing fiber and its illumination pattern on a piece of paper which has a relatively uniform light distribution.

The radial illumination pattern along the etched fiber length can be modeled as a cylindrical shape. Assuming that the output energy E_{output} from the fiber is uniformly distributed along the diffusing fiber, the fluence at distance R from the fiber position can be estimated as,

$$Fluence = \frac{E_{output}}{2\pi \cdot R \cdot l}, \tag{5}$$

where l is the length of the etched fiber. In the current design, the length of the etched fiber is 2 cm. A longer length of the diffusing fiber can also be fabricated using the same approach. In this model, the beam divergence along the longitudinal direction is neglected. Figure 3 shows how the fluence drops with increasing distance for $E_{output} = 50\,\text{mJ/pulse}$ and $l = 2\,\text{cm}$ in our design. Here Eq. (5) is a rough estimation of light fluence inside the tissue where the light distribution is assumed to be homogeneous after multiple scattering events. The region close to the fiber surface has a very high fluence due to the limited contact area. With a 25 Fr cystoscope sheath, the minimum laser-tissue contact distance is estimated to be ~5 mm. In Fig. 3, the fluence is shown to be nearly 8 mJ/cm^2 at R = 5 mm, which represents the maximum fluence on the laser-tissue contact surface. This value is well below the MPE value of 20 mJ/cm^2 (for $\lambda \leq 700$ nm). Meanwhile, the fluence drops exponentially as the distance increases. The fluence falls to 2 mJ/cm^2 at $R = 2\,\text{cm}$ distance. Due to our design of using a long section of diffusing fiber and the cystoscope sheath, the laser energy is distributed over a relatively large laser-tissue contact area and the fluence expected on the urethral wall is kept well below the laser safety limit MPE. To increase the SNR and the penetration depth, approaches of increasing the fluence are also considered. By adding a cylindrical reflection mirror which directs light to just one side of the probe, the fluence can be doubled. Furthermore, nearly one-third of the light still exits from the forward direction of the diffusing fiber, which will also be reflected to the side illumination direction.

Biomedical Optics EXPRESS

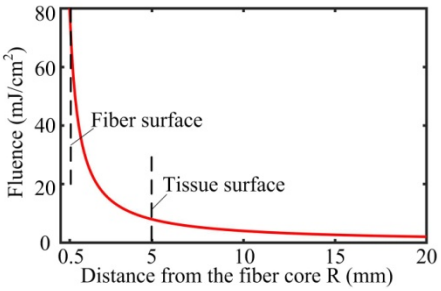

Fig. 3. Calculated fluence on a cylindrical illumination surface at various distances. The output energy from the fiber is assumed to be 50 mJ/pulse. The dash lines indicate the position of the fiber surface and the tissue surface, respectively.

2.3 Design of side reflection mirror to reshape the beam

In 360 degree radial illumination, the fluence at the far distance is relatively low. To increase the fluence, a mirror can be added along the diffusing fiber to reflect the beam to only one side which doubles the fluence as a result. Considering the geometrical characteristics of the urethra tract, a circular cylindrical mirror and a parabolic cylindrical mirror are tested and compared by simulations and experiments.

Based on optical principles, the focus of a circular cylindrical mirror only exists under paraxial condition. Comparatively, a parabolic cylindrical mirror can form an ideal parallel reflected beam. For the diffusing fiber positioned at the focus, the reflected rays by the circular cylindrical mirror and the parabolic cylindrical mirror are shown in Figs. 4(a) and 4(b), respectively. In Fig. 4(a), only the paraxial rays are collimated while the rays at large angles are slightly focused. In Fig. 4(b), all the rays reflected by the parabolic surface become collimated.

A Zemax (Zemax LLC, Washington, United States) simulation is carried out to analyze the intensity distribution of the reflected beam by the two mirrors. In the simulation, the parameters are set as $r = 2.5\,\text{mm}$ for the circular cylindrical mirror and $p = 2\,\text{mm}$ for the parabolic cylindrical mirror. Their focal distances are 1.25 mm and 1 mm, correspondingly. For both mirrors, the width along x-axis is 5 mm and the length along y-axis is 30 mm. With the same width, the height of the two mirrors are slightly different. A 20 mm long radial light source with 360 degree emission angle is placed at the focus line to simulate the diffusing fiber. Figures 4(a) and 4(b) present the cross-sectional view of the simulation with circular and parabolic cylindrical mirror respectively. Figures 4(c) and 4(d) show the intensity distribution from the two mirrors on an observation plane at 5 mm away from the fiber, which is the expected location of the laser-tissue contact surface. Figure 4(c) shows that the reflected beam is not a perfectly parallel beam but has a tendency to converge to the center. In comparison, Fig. 4(d) shows a more uniform distribution pattern. Since the rays that are above the reflection surface are not reflected by the mirror, those rays will still be diverged and super-positioned on the reflected rays from the mirror.

Biomedical Optics EXPRESS

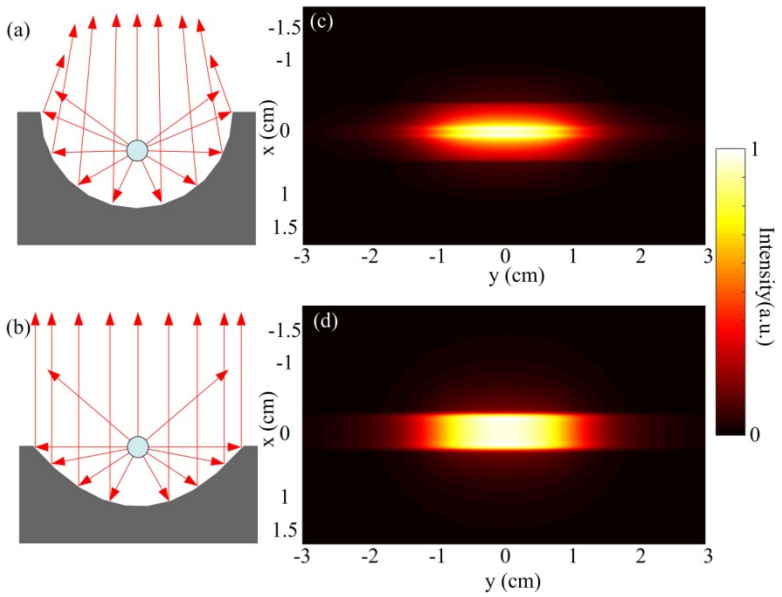

Fig. 4. Comparison of the reflection pattern. (a) and (b) are the ray tracing for the circular cylindrical mirror and the parabolic cylindrical mirror, respectively. (c) and (d) are the simulated light distribution pattern at 5 mm away from the circular cylindrical mirror and the parabolic cylindrical mirror, respectively.

For our experiments, a circular cylindrical mirror and a parabolic cylindrical mirror are fabricated by 3D printing (Shapeways, New York, United States) in premium silver which provides high reflectivity over 95%. The fabrication accuracy is around 0.1 mm. The design parameters of the mirrors in the simulation and experiment are the same. The experimental characterizations of the mirrors are shown in Fig. 5. Figure 5(a) illustrates the experimental setup for measuring the light intensity distribution. Visible light at 660-nm is coupled into the probe to display the beam distribution. The beam illumination on a piece of white paper and its intensity profile are recorded by a digital camera [25]. Figure 5(b) shows the beam intensity distribution as a function of distance for the circular cylindrical mirror and for the parabolic cylindrical mirror, respectively. The intensity is normalized between 0 to 1. Both the circular and parabolic cylindrical mirrors display a rectangular beam profile. The parabolic cylindrical mirror forms a more uniform distribution than the circular cylindrical mirror. The full width of half maximum (FWHM) of the beam size in the X and Y directions are plotted in Figs. 5(c) and 5(d), respectively, as a function of distance away from the probe. By placing the diffusing fiber at the focus of the cylindrical reflection mirror, the divergence of the beam in the X direction is reshaped into a more collimated beam. According to optical principles, the parabolic cylindrical mirror can provide a better collimation than the circular cylindrical mirror. This can be seen in Figs. 5(b) and 5(c). With the circular cylindrical mirror, the FWHM of the beam size does not change much for z less than 4 mm and then it diverges much faster than the beam reshaped by the parabolic cylindrical mirror. With the parabolic cylindrical mirror, the beam size diverges slowly. The parabolic cylindrical mirror only reflects and collimates about half of the rays emitting from the fiber. The rays that are not reflected by the mirror are still diverged which leads to the overall gradual divergence of the beam. In the Y direction, the beam size is mainly determined by the length of the diffusing fiber although some divergence is also observed. When the distance between the diffusing fiber and tissue surface is known, the beam size on the laser-tissue contact surface can be estimated based on the beam divergence shown in Fig. 5.

Biomedical Optics EXPRESS

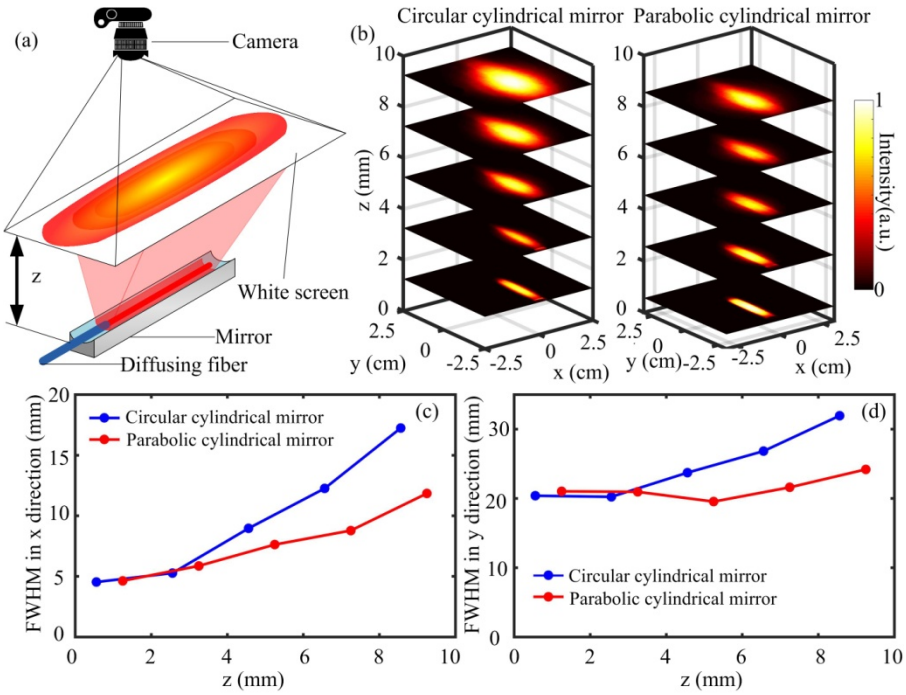

Fig. 5. Experimental results of the beam profile. (a) Illustration of the measurement setup. (b) Changes of the beam profile at various distances for the circular cylindrical mirror and the parabolic cylindrical mirror, respectively. (c) and (d) are the comparison of the FWHM of the beam profile in the x and y directions, respectively.

2.4 Characterization of the transurethral illumination probe

To redirect the light emitted from the fiber tip to the side direction of the fiber, a 45° end mirror is added to the distal end of the parabolic cylindrical mirror. The 45° end mirror reflects the residual forward propagating light to the side direction, which enhances the output energy in the side illumination. Figures 6(a) and 6(b) show the 2D beam intensity distribution with and without the end mirror, respectively, at a screen distance of 5 mm. Figures 6(c) and 6(d) compare the 1D intensity profile in the X and Y direction, respectively. The 1D profiles are extracted from Figs. 6(a) and 6(b) at the corresponding positions marked by the white arrows. Since the end mirror strengthens the light intensity at one end by reflecting the light from the fiber tip, Fig. 6(d) shows a slight non-uniform intensity distribution where the end mirror is added. In Fig. 6(c), the central beam profile with the end mirror looks similar to the profile without the end mirror in the x direction. The enhancement of the output energy from the illumination probe is also measured by a large area detection sensor (J-50MB-YAG, Coherent, CA, United States). For example, without the end mirror, the pulse energy in the side illumination is measured to be 21 mJ/pulse. With the end mirror, the output energy is improved to 28 mJ/pulse, which represents a 33% increase. From the beam intensity distribution, the illumination area at $1/e^2$ intensity is found to be around 4 cm^2 at 5 mm distance that is assumed to be the closest distance from the fiber to the tissue surface. In the following experiments, this measured beam area will be used to calculate the fluence on the laser-tissue contact surface by using the measured pulsed energy divided by the area. Due to some laser power fluctuation, the fluence value may vary accordingly.

Biomedical Optics EXPRESS

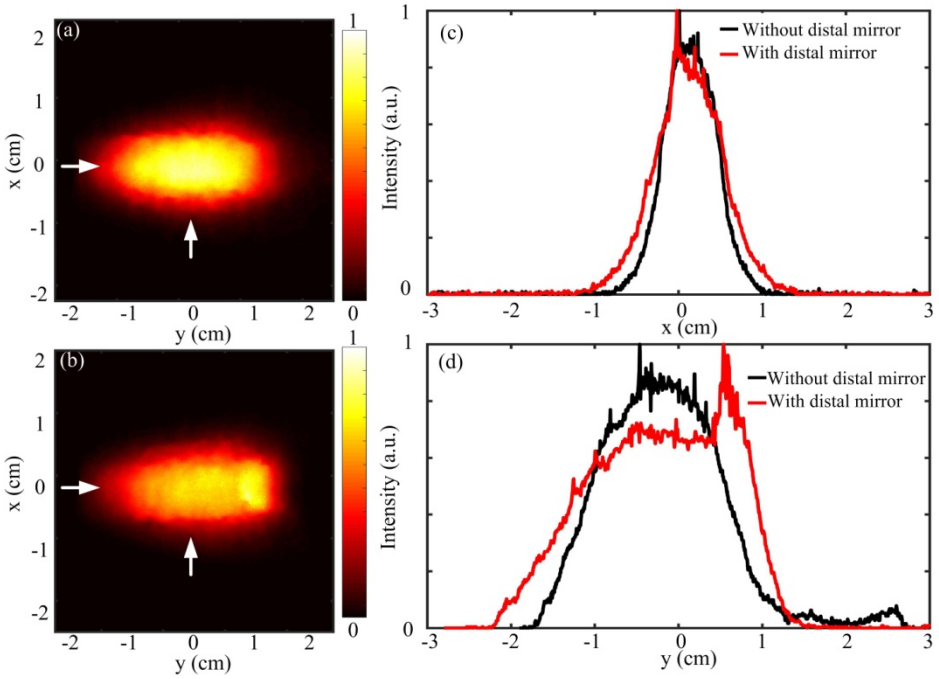

Fig. 6. Beam profile from the parabolic cylindrical mirror with and without the 45° end mirror. (a) 2D beam profile without the end mirror (b) 2D beam profile with the end mirror (c) 1D beam profile along x axis. (d) 1D beam profile along y axis. White arrows indicate the positions where the 1D profiles are extracted.

3. PAT imaging experimental results

3.1 Experimental setup

The PAT system consists a Q-switched Nd:YAG laser (Surelite OPO Plus, SLIII-10, Amplitude, San Jose, United States) and a medical ultrasound system (Ultrasonix MDP, Analogic, Richmond, Canada) [27]. The Nd:YAG laser generates 3-5 ns laser pulses at a 10 Hz repetition rate and 1064 nm wavelength. The 1064 nm wavelength is then frequency doubled to 532 nm. The 532 nm wavelength pumps an optical parametric oscillator (OPO) which generates tunable wavelength from 675 to 2500 nm. In our experiments for PAT imaging, the 700 nm wavelength is selected. To couple the laser output into a fiber, a beam homogenizer is applied to reduce the peak power on the fiber tip surface [27]. Up to 50 mJ/pulse energy can be coupled into a 1000-μm-core-diameter fiber. For receiving the PA signal, a 5-14 MHz linear transducer array with 38 mm width (L14-5/38, Analogic, Richmond, Canada) is used for general experiment and a 5-9 MHz TRUS transducer with 55 mm width (Analogic, Richmond, Canada) is used for experiment on the prostate mimicking phantom. The received signal is amplified and digitized by a data acquisition system (SonixDAQ, Analogic, Richmond, Canada). PAT images are reconstructed by delay and sum [34].

To characterize the maximum optical power that can be coupled into the 1000-μm-core-diameter fiber, the output from a cleaved fiber without the processing of diffusion tip is measured, and a 50 mJ/pulse energy is obtained. To characterize the optical power that is delivered by the diffusing fiber, the optical power from the side illumination beam and the residual forward emitted beam are measured and summed together, and a total power of 28 mJ/pulse is obtained. Several reasons may cause the power measured from the diffusing fiber to be lower than that from the unprocessed fiber. The laser coupling into the diffusing fiber may not be optimal because the power is maximized for the residual forward emitted beam,

Biomedical Optics EXPRESS

where it may not be the maximum for the side illumination beam simultaneously. Since the light emitted from the diffusing fiber is diffusing over a wide area, the power meter may not be able to capture all the emitted power in all directions. Assuming all the 50 mJ/pulse can be delivered by the diffusing fiber, the fluence on the laser-tissue contact surface would be 12.5 mJ/cm^2, which is still below the safety limit.

3.2 Human hairs inside chicken breast tissue

The transurethral illumination probe is tested by imaging human hairs embedded in chicken breast tissue. The illumination probe and the transducer are positioned face-to-face with a separation of approximately 6 cm. The fluence on the laser tissue contact surface is around 8.5 mJ/cm^2. The reconstructed PAT image of human hair is shown in Fig. 7(a). The hair can be visualized as deep as 3 cm away from the illumination probe. In Fig. 7(a), some strong PA signals are observed near the probe surface which could be artifacts. The artifacts could be due to reverberation of PA signals or strong laser fluence near the probe. The comparatively strong local fluence near the probe surface could generate strong PA signal from any absorbers in that region [19]. Higher fluence rate leads to higher SNR, but also generates strong artifacts near the illumination probe. Instead of masking out this artifact as reported in Ref. 25, an attenuation compensation method is applied to reduce this artifact [35].

In biological tissue, light intensity attenuates exponentially due to scattering and absorption. Thus, the fluence can be considered to attenuate exponentially, which can be described as [36],

$$I(z) \propto I_0 e^{-\mu_{eff} z}, \tag{6}$$

where μ_{eff} is the effective attenuation coefficient of the turbid medium and I_0 is the fluence of the incident beam. The effective attenuation is an approximation for biological tissue when the absorption is dominated by scattering and is given as [37],

$$\mu_{eff} = \sqrt{3\mu_a\left(\mu_a + \mu_s^{'}\right)} \tag{7}$$

where μ_a is the absorption coefficient and $\mu_s^{'}$ is the reduced scattering coefficient. To compensate the depth dependent signal drop due to reduced fluence at deeper penetration depth, an attenuation compensation factor $e^{\mu_{eff} z}$ can be multiplied with the received PA signal. In our study, the effective attenuation coefficient of 0.9 cm^{-1} at 650 nm in chicken breast tissue is used according to other literature reports [38]. Figure 7(b) shows the reconstructed PAT image after applying the attenuation compensation. The artifact near the illumination probe is effectively removed. Moreover, the contrast for the structures further away from the light source is greatly enhanced. A hair located 4.5 cm away from the illumination probe can be visualized, indicating good penetration depth of the PAT system.

Biomedical Optics EXPRESS

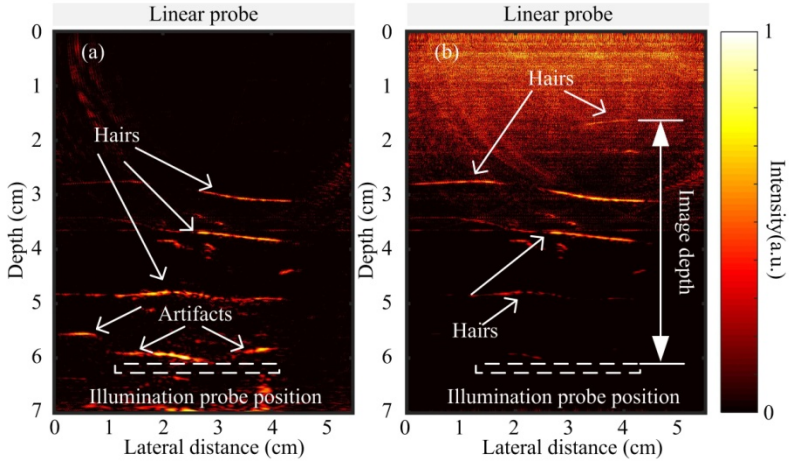

Fig. 7. PAT images of human hair embedded in chicken breast tissue. (a) Without attenuation compensation. (b) With attenuation compensation.

3.3 Prostate mimicking phantom

To evaluate the potential of the PAT system for prostate imaging, a tissue-mimicking prostate phantom was developed and imaged. The phantom was constructed to contain the specific absorption and scattering coefficients of prostate tissue which were close to the reported values of human prostate [39–41]. Several studies have characterized the optical properties of human prostate near 700 nm wavelength. Zhu *et al*. measured the reduced scattering coefficient to be 11.8 ± 8.2 cm^{-1} (range from 1.1 to 44 cm^{-1}) and the absorption coefficient to be 0.4 ± 0.2 cm^{-1} at 732 nm wavelength from 13 patients [39]. Weersink *et al*. measured the reduced scattering coefficient to be 3.4 ± 1.6 cm^{-1} and the absorption coefficient to be 0.4 ± 0.2 cm^{-1} at 762 nm wavelength from 22 patients [40]. Svensson *et al*. reported the reduced scattering coefficient to be 8.7 ± 1.9 cm^{-1} and the absorption coefficient to be 0.5 ± 0.1 cm^{-1} at 660 nm wavelength from 9 patients [41]. Thus, there seem to have a wide range and a large standard deviation due to the difference among patients and the selection of measurement locations.

Our phantom recipe includes 0.3 g agar powder, 0.3 g aluminum oxide, and 0.02 ml methylene blue in every 10 ml water. Using the inverse adding-doubling method [42], the reduced scattering coefficient and the absorption coefficient are measured to be 2.8 cm^{-1} and 0.2 cm^{-1}, respectively. The effective attenuation coefficient and the penetration depth for 1/e decay can be calculated to be 1.34 cm^{-1} and 0.75 cm, respectively [41]. Compared with the optical properties from literature, the coefficients obtained from our recipe are within the range but on the lower end. This phantom can provide a reasonable estimation of the performance of the probe in prostate tissue. The actual penetration for *in vivo* imaging of prostate will be patient dependent.

Two tube-shaped channels are created in the phantom to mimic the rectum and urethra as shown in Fig. 8(a). Between the two channels, four rows of pencil leads are placed in the middle as shown in Fig. 8(b). In imaging, the TRUS probe and illumination probe are inserted in the mimicking rectum and urethra channels, respectively. The fluence on the phantom is around 10 mJ/cm^2. The PAT image is shown in Fig. 8(c), where two rows of pencil leads which are closer to the light source can be detected. At larger depth, the fluence is largely attenuated and the SNR is very low. After applying the attenuation compensation, all the four rows of pencil leads can be clearly seen as shown in Fig. 8(d), indicting an optical penetration of ~3.5 cm.

Biomedical Optics EXPRESS

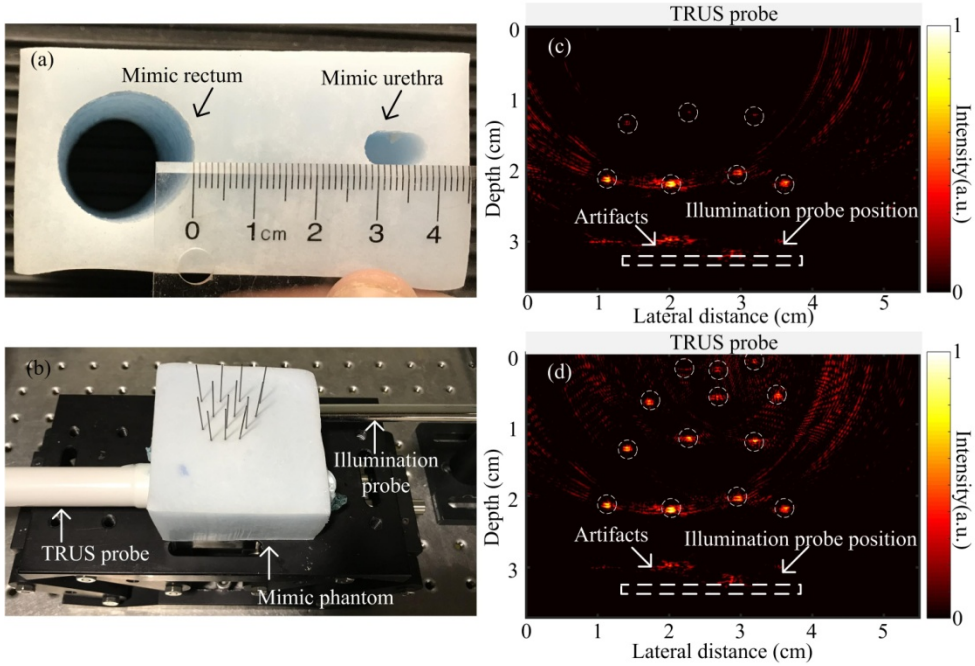

Fig. 8. PAT imaging of prostate mimicking phantom. (a) Photograph of the phantom where two tube shaped cavities indicate the location of rectum and urethra. (b) Experimental setup. (c) and (d) are the PAT images of the pencil leads embedded in the phantom without, and with attenuation compensation, respectively.

While the reflection mirror design can increase the fluence, the current transurethral illumination probe provides only one-side illumination at each laser shot. To image the structures on both sides of the probe, the transurethral illumination probe can be rotated 180° to illuminate the other side sequentially. This is tested on a prostate mimicking phantom with inserted human hairs. In the experiment, the position of the TRUS probe is fixed. By rotating the illumination probe at 0° and 180° respectively in the phantom, a forward and a backward illumination is sequentially applied to image the structures on both sides. Figures 9(a) and 9(b) show the human hairs obtained by forward and backward illumination, respectively. The hair can be resolved with better resolution in Fig. 9(a) than in 9(b) because the objects are closer to the transducer in the forward illumination. Figure 9(c) shows the combined image from both the forward and backward illumination, which is similar to the case as if the fiber probe illuminates at 360°.

For imaging the prostate, the fiber probe together with the cystoscope sheath can be inserted through urethra. The direction of the illumination beam can be controlled by rotating the cystoscope sheath to illuminate the different regions around the prostate. For 2D imaging, two rotation angles for a forward and a backward illumination will be sufficient. For 3D imaging, 3-4 rotation angles of the probe may be required in order to cover the full volume of the prostate. For receiving the PA signal, a scheme to image prostate in 3D by using a da Vinci robot to control the scanning of a linear transducer has been reported [43].

Biomedical Optics EXPRESS

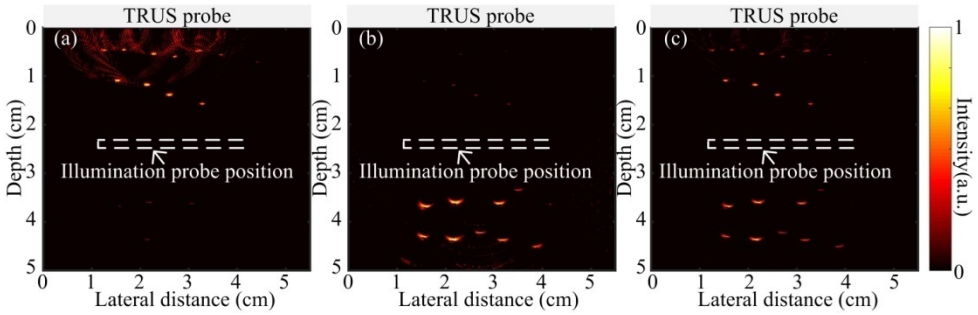

Fig. 9. PAT images of hair embedded in the prostate mimicking phantom. (a) Forward illumination where the illumination probe faces the TRUS probe. (b) Backward illumination where the illumination probe faces the opposite side of the TRUS probe. (c) Result combining (a) and (b).

4. Discussion

Our work presents a prototype transurethral illumination probe for PAT imaging of prostate. Compared to the transurethral illumination probe reported by Bell *et al.* [25], our design makes several major improvements towards translating the technology for *in vivo* imaging. A high energy of up to 50 mJ/pulse is coupled into a 1000-µm-core-diameter fiber. The high energy pulse ensures that high SNR and deep penetration can be achieved with this probe in PAT imaging. Furthermore, the laser safety limit is addressed by providing a large illumination area and controlling the fluence on the laser-tissue contact surface to be below the MPE requirement. The large illumination area is achieved by processing the fiber tip to create diffusing fiber over a few centimeters length. Thus, most of the light can be diffused to the side illumination direction. A parabolic cylindrical mirror reshapes the beam to one side of the probe for controlling the fluence and illumination pattern. Therefore, both high fluence and laser safety limit are addressed, which can potentially translate PAT for *in vivo* prostate imaging in the future.

There are several improvements that can be considered in the future to make the probe more suitable for prostate imaging in the clinic. Prostate cancer is most commonly found in elderly men, who usually have enlarged prostate caused by benign prostatic hyperplasia [29,30]. Collins *et al.* reported that the mean volume of prostate increased from 25 ml for the 40-49 age group, to 40 ml for the 70-79 age group in a study of 472 patients [30]. Eri *et al.* reported the mean anterioposterior, transverse, and cephalocaudal prostate diameters to be 3.5, 5.3, and 4.9 cm, respectively, in a patient group with average age of 70 [29]. In order to image the entire prostate in elderly patient, a pullback approach of the fiber probe can be applied, or the length of the diffusing fiber can be increased to 5 cm directly. Fabricating a 5 cm diffusing fiber can be achieved by applying the process described in Section 2.2 over a longer section of fiber. The method of using etching cream to fabricate the diffusing fiber is not limited on the fiber length. The etched fiber is only slightly reduced in its diameter and the strength of the fiber is maintained.

In the prototype, the probe is inserted in a cystoscope sheath of 25 Fr (8.3 mm diameter). For standard diagnostic cystoscopy, 21-22 Fr (7-7.3 mm diameter) rigid cystoscopes are most frequently used. Intravenous sedation or regional anesthesia is required when a rigid cystoscopy is applied. Application of a larger diameter rigid cystoscopy only occurs in some particular cases which require general anesthesia [44]. To reduce the probe diameter to 21 Fr, the 1000-µm-core-diameter fiber can still be used but the size of the parabolic cylindrical mirror needs to be reduced. This will decrease the beam size and result in higher fluence. To keep the fluence below the MPE, the length of the diffusing fiber can be increased to illuminate over a longer beam pattern. Compared to the 5.3 mm diameter urinary catheter reported by Bell *et al.* [25], our probe size is slightly larger. Although smaller diameter

Biomedical Optics EXPRESS

catheter brings more comfort to patient, the larger diameter catheter is necessary where higher energy and larger illumination area are needed for imaging the entire prostate.

The current beam profile is not completely uniform, especially near the tip of the fiber probe where the end mirror reflects the forward emitted light to the side direction of the fiber. Non-uniform beam pattern could limit the maximum energy that can be delivered to the tissue in order to satisfy the MPE requirement everywhere. To reduce the power emitted from the forward direction and to increase the uniformity of the illumination pattern, the length of the diffusing fiber can be increased, where a larger fraction of the light will be diffused to the side illumination and only a smaller fraction will emit from the forward direction of the fiber. The side firing conversion efficiency could be further improved by extending the duration of the etching process, increasing the coupling angle [32], or reducing the fiber diameter gradually by tapering the fiber at the tip. For the remaining small fraction of the forward emitting light, the 45° end mirror can redirect those light to the side illumination and a rough surface can be processed on the end mirror to create diffuse reflection which can further improve the beam uniformity.

The fiber probe is housed in a rigid cystoscope sheath which protects and provides support to the fiber. During insertion of the cystoscope in urethra, urine can flow in the device. Although urine will not likely affect the optical property of the probe, the probe will be in direct contact with the urine. Future improvement on the probe can be achieved by adding a quartz tube to protect the diffusing fiber. Similar designs have been reported by Bell *et al*. in their transurethral illumination catheter [25] and by Li *et al.* in their internal illumination PAT [45]. Adding a quartz tubing will isolate the fiber from direct contact with the tissue, which can protect the fiber from breaking. Furthermore, it will make sterilization of the probe easier and reusing of the probe possible after each operation.

With the improved probe, PAT imaging of prostate cancer will be carried out in the future. PAT imaging will be used to detect the neurovascular bundles and microvessel structures in prostate. Detecting the extension and proximity to critical structures such as the neurovascular bundles during radical prostatectomy is critical for ensuring surgical outcomes and maintaining normal organ functions. Detecting and quantifying the microvessel structures can potentially differentiate prostate cancer from normal tissues.

Previously, the functional US and MRI techniques for quantifying MVD have shown limitations due to their low sensitivity and difficulty in discriminating cancer from highly vascularized benign prostate hyperplasia [29,30]. Rubin *et al*. assessed MVD in one hundred radical prostatectomy specimens by comparing pathologic results with the intra-observer MVD counting results [46]. The study found that MVD was not associated with Gleason sum, tumor stage, surgical margin status or seminal vesicle invasion. In a study by Mucci *et al*. [47], the histopathologic measure of MVD on the serial sections of the prostatectomy from 572 patients diagnosed with prostate cancer showed that MVD was not linked to cancer-specific mortality. Instead, the vascular size and irregularity was found to be strong predictors of the fatal disease.

With its high sensitivity, PAT could provide more information about the microvessel structures. In Ref. 20, Horiguchi *et al*. analyzed the correlation of PA signal intensity with the MVD, total vascular area (TVA) and total vascular length (TVL) that were measured by histopathology in three prostate cancer patients. The histological examination showed that TVA and TVL were larger and longer in the peritumoral area of the tumor than in the index tumor. The areas with high PA intensity correlated well with regions that have greater TVA and TVL. High PA intensity correlated with high MVD region in one patient. Furthermore, other quantitative analysis can also be carried out based on the radio frequency (RF) spectrum of PA signal because the PA signal frequency is sensitive to the size of the absorbers. Sinha *et al*. [48] and Huang *et al*. [49] have demonstrated the feasibility of identifying the size of the absorber by analyzing PA signal in the frequency domain. The evaluation of PA signals in the frequency domain might show useful information about the size of the microvessels.

Biomedical Optics EXPRESS

Therefore, PAT has a great potential for improving prostate cancer imaging by detecting and analyzing multiple characteristics of the microvessels, including MVD, area and length of microvascular structure, and size of microvessels.

5. Conclusion

A transurethral illumination probe was designed for PAT imaging of prostate. The probe contained a radially illuminating diffusing fiber of 2 cm length. The radial illumination was reflected and reshaped by a parabolic cylindrical mirror to obtain nearly parallel side illumination with doubled fluence. The fiber assembly was inserted into a 25 Fr cystoscope sheath to provide protection of the fiber and a minimal laser-tissue contact distance of 5 mm. Due to the unique design of the illumination probe, a 4 cm^2 laser-tissue contact surface was obtained and the fluence was kept below the MPE. The illumination probe was evaluated using tissue phantoms and prostate mimicking phantoms. A 3.5 cm penetration depth in the prostate mimicking phantom was demonstrated using 10 mJ/cm^2 fluence at 700 nm wavelength. An approach of acquiring PAT image from both sides of the probe was also demonstrated by rotating the illumination probe at 0° and 180° for a forward and a backward illumination, respectively. The deep penetration ability makes PAT imaging of the entire prostate possible. This technique can potentially be applied for PCa detection and image-guided targeted biopsy.

Funding

Natural Sciences and Engineering Research Council of Canada (NSERC), Collaborative Health Research Project (CHRP 446576-13); Canadian Institutes of Health Research (CIHR), Collaborative Health Research Project (CPG-127772).

Acknowledgments

The authors would like to thank Dr. Chris Nguan for useful discussion and a helping hand.

Disclosures

The authors declare that there are no conflicts of interest related to this article.

References

1. R. L. Siegel, K. D. Miller, and A. Jemal, "Cancer statistics, 2018," CA Cancer J. Clin. **68**(1), 7–30 (2018).
2. A. Heidenreich, P. J. Bastian, J. Bellmunt, M. Bolla, S. Joniau, T. van der Kwast, M. Mason, V. Matveev, T. Wiegel, F. Zattoni, and N. Mottet, "EAU guidelines on prostate cancer. part 1: screening, diagnosis, and local treatment with curative intent-update 2013," Eur. Urol. **65**(1), 124–137 (2014).
3. F. H. Schröder, P. van der Maas, P. Beemsterboer, A. B. Kruger, R. Hoedemaeker, J. Rietbergen, and R. Kranse, "Evaluation of the digital rectal examination as a screening test for prostate cancer. Rotterdam section of the European Randomized Study of Screening for Prostate Cancer," J. Natl. Cancer Inst. **90**(23), 1817–1823 (1998).
4. W. J. Catalona, J. P. Richie, F. R. Ahmann, M. A. Hudson, P. T. Scardino, R. C. Flanigan, J. B. DeKernion, T. L. Ratliff, L. R. Kavoussi, B. L. Dalkin, W. B. Waters, M. T. MacFarlane, and P. C. Southwick, "Comparison of digital rectal examination and serum prostate specific antigen in the early detection of prostate cancer: results of a multicenter clinical trial of 6,630 men," J. Urol. **151**(5), 1283–1290 (1994).
5. M. Noguchi, T. A. Stamey, J. E. McNeal, and C. M. Yemoto, "Relationship between systematic biopsies and histological features of 222 radical prostatectomy specimens: lack of prediction of tumor significance for men with nonpalpable prostate cancer," J. Urol. **166**(1), 104–110 (2001).
6. B. Djavan, V. Ravery, A. Zlotta, P. Dobronski, M. Dobrovits, M. Fakhari, C. Seitz, M. Susani, A. Borkowski, L. Boccon-Gibod, C. C. Schulman, and M. Marberger, "Prospective evaluation of prostate cancer detected on biopsies 1, 2, 3 and 4: when should we stop?" J. Urol. **166**(5), 1679–1683 (2001).
7. E. D. Nelson, C. B. Slotoroff, L. G. Gomella, and E. J. Halpern, "Targeted biopsy of the prostate: the impact of color Doppler imaging and elastography on prostate cancer detection and Gleason score," Urology **70**(6), 1136–1140 (2007).
8. M. Kongnyuy, A. K. George, A. R. Rastinehad, and P. A. Pinto, "Magnetic resonance imaging-ultrasound fusion-guided prostate biopsy: review of technology, techniques, and outcomes," Curr. Urol. Rep. **17**(4), 32 (2016).

Biomedical Optics EXPRESS

9. C. M. Hoeks, J. O. Barentsz, T. Hambrock, D. Yakar, D. M. Somford, S. W. Heijmink, T. W. Scheenen, P. C. Vos, H. Huisman, I. M. van Oort, J. A. Witjes, A. Heerschap, and J. J. Fütterer, "Prostate cancer: multiparametric MR imaging for detection, localization, and staging," Radiology **261**(1), 46–66 (2011).
10. K. M. Pondman, J. J. Fütterer, B. ten Haken, L. J. Schultze Kool, J. A. Witjes, T. Hambrock, K. J. Macura, and J. O. Barentsz, "MR-guided biopsy of the prostate: an overview of techniques and a systematic review," Eur. Urol. **54**(3), 517–527 (2008).
11. G. Russo, M. Mischi, W. Scheepens, J. J. De la Rosette, and H. Wijkstra, "Angiogenesis in prostate cancer: onset, progression and imaging," BJU Int. **110**(11c), E794–E808 (2012).
12. A. Postema, M. Mischi, J. de la Rosette, and H. Wijkstra, "Multiparametric ultrasound in the detection of prostate cancer: a systematic review," World J. Urol. **33**(11), 1651–1659 (2015).
13. R. Alonzi, A. R. Padhani, and C. Allen, "Dynamic contrast enhanced MRI in prostate cancer," Eur. J. Radiol. **63**(3), 335–350 (2007).
14. G. J. Jager, E. T. Ruijter, C. A. van de Kaa, J. J. de la Rosette, G. O. Oosterhof, J. R. Thornbury, and J. O. Barentsz, "Local staging of prostate cancer with endorectal MR imaging: correlation with histopathology," AJR Am. J. Roentgenol. **166**(4), 845–852 (1996).
15. L. V. Wang and S. Hu, "Photoacoustic tomography: *in vivo* imaging from organelles to organs," Science **335**(6075), 1458–1462 (2012).
16. A. Ng and J. Swanevelder, "Resolution in ultrasound imaging," Contin. Educ. Anaesth. Crit. Care Pain **11**(5), 186–192 (2011).
17. V. G. Andreev, A. E. Ponomarev, P. M. Henrichs, M. Motamedi, E. Orihuela, E. Eyzaguirre, and A. A. Oraevsky, "Detection of prostate cancer with opto-acoustic tomograph," In Biomedical Optoacoustics IV **4960**, 45–58 (2003).
18. X. Wang, W. W. Roberts, P. L. Carson, D. P. Wood, and J. B. Fowlkes, "Photoacoustic tomography: a potential new tool for prostate cancer," Biomed. Opt. Express **1**(4), 1117–1126 (2010).
19. A. Horiguchi, K. Tsujita, K. Irisawa, T. Kasamatsu, K. Hirota, M. Kawaguchi, M. Shinchi, K. Ito, T. Asano, H. Shinmoto, H. Tsuda, and M. Ishihara, "A pilot study of photoacoustic imaging system for improved real-time visualization of neurovascular bundle during radical prostatectomy," Prostate **76**(3), 307–315 (2016).
20. A. Horiguchi, M. Shinchi, A. Nakamura, T. Wada, K. Ito, T. Asano, H. Shinmoto, H. Tsuda, and M. Ishihara, "Pilot Study of Prostate Cancer Angiogenesis Imaging Using a Photoacoustic Imaging System," Urology **108**, 212–219 (2017).
21. J. L. Su, R. R. Bouchard, A. B. Karpiouk, J. D. Hazle, and S. Y. Emelianov, "Photoacoustic imaging of prostate brachytherapy seeds," Biomed. Opt. Express **2**(8), 2243–2254 (2011).
22. M. A. Lediju Bell, N. P. Kuo, D. Y. Song, J. U. Kang, and E. M. Boctor, "*In vivo* visualization of prostate brachytherapy seeds with photoacoustic imaging," J. Biomed. Opt. **19**(12), 126011 (2014).
23. S. Tang, J. Chen, P. Samant, K. Stratton, and L. Xiang, "Transurethral photoacoustic endoscopy for prostate cancer: A simulation study," IEEE Trans. Med. Imaging **35**(7), 1780–1787 (2016).
24. D. Peng, Y. Peng, J. Guo, and H. Li, "Laser Illumination Modality of Photoacoustic Imaging Technique for Prostate Cancer," J. Phys. **679**(1), 012026 (2016).
25. M. A. Lediju Bell, X. Guo, D. Y. Song, and E. M. Boctor, "Transurethral light delivery for prostate photoacoustic imaging," J. Biomed. Opt. **20**(3), 036002 (2015).
26. American National Standards Institute, Safe Use of Lasers, ANSI Z136.1–2000, (Laser Institute of America, 2000).
27. M. Ai, W. Shu, T. Salcudean, R. Rohling, P. Abolmaesumi, and S. Tang, "Design of high energy laser pulse delivery in a multimode fiber for photoacoustic tomography," Opt. Express **25**(15), 17713–17726 (2017).
28. M. Mitterberger, W. Horninger, F. Aigner, G. M. Pinggera, I. Steppan, P. Rehder, and F. Frauscher, "Ultrasound of the prostate," Cancer Imaging **10**(1), 40–48 (2010).
29. L. M. Eri, H. Thomassen, B. Brennhovd, and L. L. Håheim, "Accuracy and repeatability of prostate volume measurements by transrectal ultrasound," Prostate Cancer Prostatic Dis. **5**(4), 273–278 (2002).
30. G. N. Collins, R. J. Lee, G. B. McKelvie, A. C. N. Rogers, and M. Hehir, "Relationship between prostate specific antigen, prostate volume and age in the benign prostate," Br. J. Urol. **71**(4), 445–450 (1993).
31. T. H. Nguyen, Y. H. Rhee, J. C. Ahn, and H. W. Kang, "Circumferential irradiation for interstitial coagulation of urethral stricture," Opt. Express **23**(16), 20829–20840 (2015).
32. B. Bungart, Y. Cao, T. Yang-Tran, S. Gorsky, L. Lan, D. Roblyer, M. O. Koch, L. Cheng, T. Masterson, and J. X. Cheng, "Cylindrical illumination with angular coupling for whole-prostate photoacoustic tomography," Biomed. Opt. Express **10**(3), 1405–1419 (2019).
33. M. A. Kosoglu, R. L. Hood, J. H. Rossmeisl, Jr., D. C. Grant, Y. Xu, J. L. Robertson, M. N. Rylander, and C. G. Rylander, "Fiberoptic microneedles: Novel optical diffusers for interstitial delivery of therapeutic light," Lasers Surg. Med. **43**(9), 914–920 (2011).
34. M. Xu and L. V. Wang, "Universal back-projection algorithm for photoacoustic computed tomography," Phys. Rev. E Stat. Nonlin. Soft Matter Phys. **71**(1 Pt 2), 016706 (2005).
35. S. Bu, Z. Liu, T. Shiina, K. Kondo, M. Yamakawa, K. Fukutani, Y. Someda, and Y. Asao, "Model-based reconstruction integrated with fluence compensation for photoacoustic tomography," IEEE Trans. Biomed. Eng. **59**(5), 1354–1363 (2012).
36. R. A. Kruger, P. Liu, Y. R. Fang, and C. R. Appledorn, "Photoacoustic ultrasound (PAUS)-reconstruction tomography," Med. Phys. **22**(10), 1605–1609 (1995).

Biomedical Optics EXPRESS

37. W. Cheong, S. Prahl, and A. Welch, "A review of the optical properties of biological," IEEE J. Quantum Electron. **26**(12), 2166–2185 (1990).
38. G. Marquez, L. V. Wang, S. P. Lin, J. A. Schwartz, and S. L. Thomsen, "Anisotropy in the absorption and scattering spectra of chicken breast tissue," Appl. Opt. **37**(4), 798–804 (1998).
39. T. C. Zhu, A. Dimofte, J. C. Finlay, D. Stripp, T. Busch, J. Miles, R. Whittington, S. B. Malkowicz, Z. Tochner, E. Glatstein, and S. M. Hahn, "Optical properties of human prostate at 732 nm measured in mediated photodynamic therapy," Photochem. Photobiol. **81**(1), 96–105 (2005).
40. R. A. Weersink, A. Bogaards, M. Gertner, S. R. Davidson, K. Zhang, G. Netchev, J. Trachtenberg, and B. C. Wilson, "Techniques for delivery and monitoring of TOOKAD (WST09)-mediated photodynamic therapy of the prostate: clinical experience and practicalities," J. Photochem. Photobiol. B **79**(3), 211–222 (2005).
41. T. Svensson, S. Andersson-Engels, M. Einarsdóttír, and K. Svanberg, "*In vivo* optical characterization of human prostate tissue using near-infrared time-resolved spectroscopy," J. Biomed. Opt. **12**(1), 014022 (2007).
42. S. A. Prahl, M. J. C. van Gemert, and A. J. Welch, "Determining the optical properties of turbid mediaby using the adding-doubling method," Appl. Opt. **32**(4), 559–568 (1993).
43. H. Moradi, S. Tang, and S. E. Salcudean, "Toward intra-operative prostate photoacoustic imaging: configuration evaluation and implementation using the da Vinci research kit," IEEE Trans. Med. Imaging **38**(1), 57–68 (2019).
44. D. Georgescu, E. Alexandrescu, R. Multescu, and B. Geavlete, "Cystoscopy and urinary bladder anatomy," in *Endoscopic Diagnosis and Treatment in Urinary Bladder Pathology,* P. A. Geavlete, ed. (Elsevier Inc., 2016).
45. M. Li, B. Lan, W. Liu, J. Xia, and J. Yao, "Internal-illumination photoacoustic computed tomography," J. Biomed. Opt. **23**(3), 1–4 (2018).
46. M. A. Rubin, M. Buyyounouski, E. Bagiella, S. Sharir, A. Neugut, M. Benson, A. de la Taille, A. E. Katz, C. A. Olsson, and R. D. Ennis, "Microvessel density in prostate cancer: lack of correlation with tumor grade, pathologic stage, and clinical outcome," Urology **53**(3), 542–547 (1999).
47. L. A. Mucci, A. Powolny, E. Giovannucci, Z. Liao, S. A. Kenfield, R. Shen, M. J. Stampfer, and S. K. Clinton, "Prospective study of prostate tumor angiogenesis and cancer-specific mortality in the health professionals follow-up study," J. Clin. Oncol. **27**(33), 5627–5633 (2009).
48. S. Sinha, N. A. Rao, B. K. Chinni, and V. S. Dogra, "Evaluation of frequency domain analysis of a multiwavelength photoacoustic signal for differentiating malignant from benign and normal prostates: *ex vivo* study with human prostates," J. Ultrasound Med. **35**(10), 2165–2177 (2016).
49. S. Huang, Y. Qin, Y. Chen, J. Pan, C. Xu, D. Wu, W. Y. Chao, J. T. Wei, S. A. Tomlins, X. Wang, J. B. Fowlkes, P. L. Carson, Q. Cheng, and G. Xu, "Interstitial assessment of aggressive prostate cancer by physio-chemical photoacoustics: An *ex vivo* study with intact human prostates," Med. Phys. **45**(9), 4125–4132 (2018).